ADVANCED ENGINEERING MATERIALS

Full Papers www.aem-journal.com

# Sound Transmission Loss Enhancement in an Inorganic-Organic Laminated Wall Panel Using Multifunctional Low-Density Nanoporous Polyurea Aerogels: Experiment and Modeling

Sadeq Malakooti, Habel Gitogo Churu, Alison Lee, Saman Rostami, Samuel John May, Suzie Ghidei, Fen Wang, Qun Lu, Huiyang Luo, Ning Xiang, Chariklia Sotiriou-Leventis, Nicholas Leventis, and Hongbing Lu\*

Recently, the authors have reported an exceptional normal incidence sound transmission loss characteristic for a class of low density, highly porous, and mechanically strong polyurea aerogels. Herein, a laminated composite comprising the organic low-density aerogels bonded with an inorganic compound (e.g., gypsum materials) is considered to investigate the constrained damping effects of the aerogels on the airborne sound insulation behavior of the composite using the standard chamber-based diffuse sound field measurements. Huge improvement in the sound transmission loss is obtained due to the use of aerogel without a significant increase in the overall weight and thickness of the composite panel (e.g., more than 10 dB increase by reaching 40 dB sound transmission loss at 2 kHz after the implementation of only two 5 mm-thick aerogel layers at bulk densities 0.15 and 0.25 g cm<sup>-3</sup>). This uncommon behavior breaks the empirical "Mass Law" nature of the most conventional acoustic materials. In addition, an exact analytical time-harmonic plane-strain solution for the diffused wave propagation through the multilayered structure is provided using theories of linear elasticity and Biot's dynamic poroelasticity. The theoretical results are well supported by the experiments which can be utilized for the design of the future light-weight multifunctional composite structures.

Prof. H. Lu, Dr. H. Luo, S. Malakooti, S. Rostami, S. J. May, S. Ghidei Department of Mechanical Engineering, The University of Texas at Dallas, Richardson, TX 75080, USA

E-mail: hongbing.lu@utdallas.edu

Dr. H. G. Habel

Department of Mechanical Engineering, LeTourneau University, Longview, TX 75602, USA

A. Lee

AVL Test Systems Inc., Plymouth, MI 48170, USA

F. Wang, Q. Lu

Nashi-Tech New Materials, Inc. 18 Zhilan Road, Nanjing, China 211100

Prof. N. Xiang

Graduate Program in Architectural Acoustics, Rensselaer Polytechnic Institute, Troy, NY 12180, USA

Prof. C. Sotiriou-Leventis, Prof. N. Leventis Department of Chemistry, Missouri University of Science and Technology, Rolla, MO 65409, USA

DOI: 10.1002/adem.201700937

## 1. Introduction

Multifunctional composites play a pivotal role in the pursuit of simultaneous improvements in various materials properties such as ductility, vibro-acoustical damping, load-bearing capacity, fracture toughness, and thermal conductivity.[1,2] For instance, fiber/nanotube-reinforced polymer and ceramic-matrix composites have been widely used in load-bearing applicy ations.[3] That combination of materials tries to address the typical conflicting engineering requirement encountered in numerous circu mstances (e.g., light structure engineering applications, aeronautical, and aerospace technologies), which are lightweight and mechanical strength.<sup>[4]</sup> Aerogels are multifunctional low-density, highly porous materials with the potential to be the ultimate approach to the optimal combination of lightweight and strength.<sup>[5]</sup>

Conventionally, aerogels were associated with silica and they were produced by drying wet silica gels by converting their pore filling liquid into a supercritical fluid.<sup>[5,6]</sup> Owing to their extremely low thermal conductivity and relatively low speed of sound, [7] silica aerogels have been implemented successfully in thermal insulation.<sup>[8,9]</sup> However, silica aerogels are also fragile materials and unsuitable for handling as required by most applications. That limitation has been addressed by introducing polymer cross-linked silica aerogels (known as Xaerogels), whereas a nano-thin polymer coating covered conformally the entire skeletal framework of conventional silica aerogels. The density increased by only a factor of 2-3 (still very lightweight materials), but the ultimate strength increased by a factor of 300. [10] Subsequently, it was reasoned that since the exceptional mechanical strength of X-aerogels was attributed to the polymer coating, purely polymeric aerogels with the same nanostructure and interparticle connectivity of X-aerogels would have similar mechanical properties.<sup>[11]</sup> That hypothesis has been confirmed with purely polymeric aerogels from all major polymeric classes such as polyureas, [12] polyurethanes, [13]



www.aem-iournal.com

ADVANCED ENGINEERING MATERIALS

polyimides,<sup>[14]</sup> and polyamides (KevlarTM-like).<sup>[15]</sup> Indeed, new applications that were previously unrelated to aerogels, as in ballistic protection (armor), have now become feasible.<sup>[16]</sup>

Focusing on polyurea (PUA) aerogels, from a reaction of isocyanate and water, our co-author could conveniently prepare the PUA aerogels at high porosity (up to 98.6% v/v) and low density  $(0.016-0.55\,\mathrm{g\,cm^{-3}})$ . The Young's modulus, ultimate stress, and strain for the PUA aerogels were up to 300 MPa, 631 MPa, and 88%, respectively, at densities lower than  $0.5\,\mathrm{g\,cm}^{-3}$  which indicate a high level of ductility and loadbearing capacity for these low-density materials. [12] Recently, we also discovered exceptionally high normal incidence sound transmission loss (STL) properties for these PUA aerogels. [17,18] The STL values were reached up to 40 dB, in contrast to traditional acoustics materials, such as polyurethane foam, which can only reach up to 5 dB.[18] Furthermore, despite most passive materials (e.g., open-celled materials), which have weak acoustic performance in sonic absorption at low frequency range (i.e., less than 5 kHz), [19] the aerogels showed remarkably high acoustic absorption and attenuation over the entire low frequency range. Such a great attribute originates from the random multiscale heterogeneous structural elements and hierarchical porosities of the aerogels which provide highly tortuous flow streams for air molecules. All these synergistic dynamic mechanisms would eventually yield to a broadband acoustic attenuation which make the aerogels unique for sound proofing applications. Due to these vast and various interesting behaviors and characteristics, we can outline the PUA aerogels to be named as a truly "Multifunctional Material".

Excitingly enough, it is natural now to investigate the aerogels in a composite arrangement (e.g., a laminated composite configuration) to have further analysis towards more advanced engineering application purposes. Accordingly, aerogel materials (i.e., in the form of thin sheets) were synthesized at different dimensions, bulk densities, and porosities. The thin aerogel sheets were then integrated between two gypsum wallboards which are used commonly in sound proofing applications. Standard field acoustic measurements were carried out to study the effects of aerogel constraint properties on the airborne sound insulation characteristics of the sandwich structures. Finally, the experimental results were further studied by comparing with theoretical predictions obtained from an exact analytical wave propagation approach based on Biot's dynamic poroelasticity and linear elasticity.

#### 2. Experimental Section

#### 2.1. Preparation and Characterization of PUA Aerogels

Here, the PUA aerogels were prepared according to the previous procedures published by the co-authors. [12] For this study, aerogels were synthesized at two different bulk densities ( $\rho_b$ ) at 0.15 and 0.25 g cm<sup>-3</sup>, which were measured from the mass and the physical dimensions of the samples. Skeletal densities ( $\rho_s$ ) were considered equal to 1.24 g cm<sup>-3</sup> at all bulk densities. [12] The aerogel porosities (h) were estimated using  $h=100\times \left[(\rho_s-\rho_b)/\rho_s\right]$  to be approximately 88 and 80% at bulk densities of 0.15 and 0.25 g cm<sup>-3</sup>, respectively. The morphology of the aerogels was determined with

SEM images taken from Au-coated samples on a Hitachi model S-4700 field emission microscope.

#### 2.2. Preparation of Laminated Composites

The general layer-by-layer approach was used for the preparation of the composite samples. The polyurea gel panels were dried in ambient conditions to form 5 mm-thick aerogel sheets (using a drum sander, the surface of all PUA aerogel samples were sanded in order to obtain a flat panel with a uniform 5 mm thickness across the entire area). Two aerogel materials with different densities were then bonded together and the combination were later integrated between two gypsum wallboards of uniform thickness of 10 mm. The bulk density of the gypsum material was 1 g cm<sup>-3</sup>. All layers were glued together using a thin layer of green glue material (The Green Glue Company). The acoustical properties of this arrangement were compared with a reference sample including only two similar gypsum wallboards of same thickness and density, bonded together using the same green glue. Two sets of samples were prepared at two different dimensions. The first and second sample sets were prepared with incidence areas of 1 and 10 m<sup>2</sup>, respectively. The larger samples were prepared by consolidating of the smaller sized samples (see Figure 1). In order to minimize the possible ageing effects on the preparation of the large sample, the aerogels were prepared in a parallel manner under controlled environmental condition (temperature below 27 °C, and the relative humidity below 70%.). The longest ageing time difference between the samples was only in the order of a few days.

#### 2.3. Airborne Sound Transmission Loss Measurements

The measurements were carried out in compliance with ASTM standard E90<sup>[20]</sup> (similar to ISO 140<sup>[21]</sup>). In this experiment, the test sample is placed at the opening of two adjacent reverberation rooms. The sample is excited by a diffuse incident sound field from one side and the radiated sound pressure levels in the other room are measured. The airborne sound transmission loss is then calculated based on the sound pressure levels in both rooms, the sound absorption in the receiving room and the incidence area of the sample. The measurement frequency range was set to 100-5000 Hz. The experiments were arranged in a way that the main sound transmission path is through the test samples. Therefore, in the case of 1 m<sup>2</sup> test sample, the rooms were only connected with an open window area where the test sample was located. While, for the 10 m<sup>2</sup> test sample, the rooms were separated by the test sample itself generating a wall between the two rooms. Figure 1a-f show the process of experimental sample and setup preparations.

# 3. Analytical Modeling

The 3D coupled structural-acoustic problem can be simplified with a 2D plane strain problem in order to construct an analytical framework for the STL characteristics of the layered structure. Therefore, in this section, the required essential core

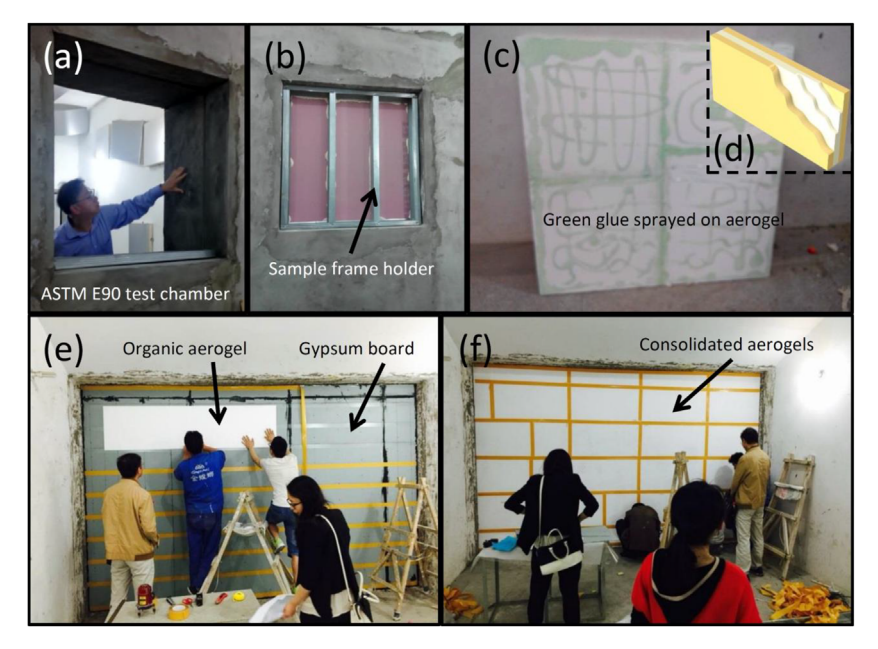


**Figure 1.** a) A view from the connecting window of the ASTM E90 test chamber prepared for a  $1\,\mathrm{m}^2$  test specimen; b)  $1\,\mathrm{m}^2$  test sample installation using sample frame holders in compliance with ASTM E90; c) A view from an aerogel panel sprayed with green glue before bonding to the another layer; d) An schematic for the final configuration of the composite sample including two gypsum skin layers (shown in yellow color) accompanied with two core aerogel layers (shown in white color); e)  $10\,\mathrm{m}^2$  composite sample preparation by consolidating several smaller aerogel samples using double sided tapes and green glue; f) A view from a  $10\,\mathrm{m}^2$  aerogel layer.

formulations in the context of the standard theoretical acoustics coupled with the theories of linear elasticity and Biot's dynamic poroelasticity will be summarized.

The problem geometry is depicted in **Figure 2** where the Cartesian coordinate system is  $\{o, x, y, z\}$ . A semi-infinite multilayered plate is submerged in an unbounded inviscid acoustic medium and  $\gamma$ -axis is normal to the plate boundary. The multilayered plate contains two isotropic linear elastic layers at the top and the bottom, and two poroelastic interlayers in between. Here, it is assumed that all layers are perfectly bonded together and a time-harmonic incident plane acoustic wave at an angle  $\theta$  with respect to  $\gamma$ -axis is impinging to the plate. The time dependency term (i.e.,  $e^{i\omega t}$ ) is suppressed throughout for the simplicity.

### 3.1. Acoustic Fluid Medium

Using standard acoustic field equations, the normal fluid velocity and the acoustic pressure in the fluid mediums 1 and 2 can be expressed in terms of the incident, reflected, and transmitted acoustic wave amplitudes (i.e.,  $I_I$ ,  $I_R$ , and  $I_T$ , respectively), as follows<sup>[22]</sup>:

$$\nu_{\gamma}^{(F_1)} = \mathrm{i} k_{\gamma} \mathrm{e}^{-\mathrm{i} k_{x} x} \left( I_{I} \mathrm{e}^{-\mathrm{i} k_{\gamma} \gamma} - I_{R} \mathrm{e}^{\mathrm{i} k_{\gamma} \gamma} \right), \tag{1}$$

$$v_{\nu}^{F_2} = ik_{\nu}I_T e^{-i\left(k_x x + k_{\nu} \gamma\right)}, \tag{2}$$

and

$$p^{(F_1)} = i\omega \rho_F e^{-ik_x x} \left( I_I e^{-ik_y y} + I_R e^{ik_y y} \right), \tag{3}$$

$$p^{(F_2)} = i\omega \rho_{\scriptscriptstyle E} I_T e^{-i(k_x x + k_y y)}, \tag{4}$$

where  $v_{\gamma}^{(F_1)}$  and  $v_{\gamma}^{(F_2)}$  are the normal fluid velocities,  $p^{(F_1)}$  and  $p^{(F_2)}$  are the acoustic pressures in the fluid mediums 1 and 2, respectively,  $\rho_F$  is the fluid density,  $k_x = k \sin\theta$  and  $k_{\gamma} = k \cos\theta$  are the wave numbers in x-and  $\gamma$ -directions,  $k = \omega/c_0$  is the acoustic wave number,  $\omega$  is the circular frequency, and  $c_0$  is the speed of sound in the fluid mediums.

#### 3.2. Isotropic Linear Elastic Medium

Using elastic wave potential technique following from the Helmholtz theorem, the wave propagation in homogenous isotropic linear elastic mediums can be analytically characterized.<sup>[23]</sup> In this context, considering the plane strain condition, the displacements (i.e.,

 $u_x^{(E)}$  and  $u_y^{(E)}$ ) and stresses (i.e.,  $\sigma_{yy}^{(E)}$  and  $\sigma_{xy}^{(E)}$ ) for an isotropic linear elastic medium can be written in terms of the propagated P- and

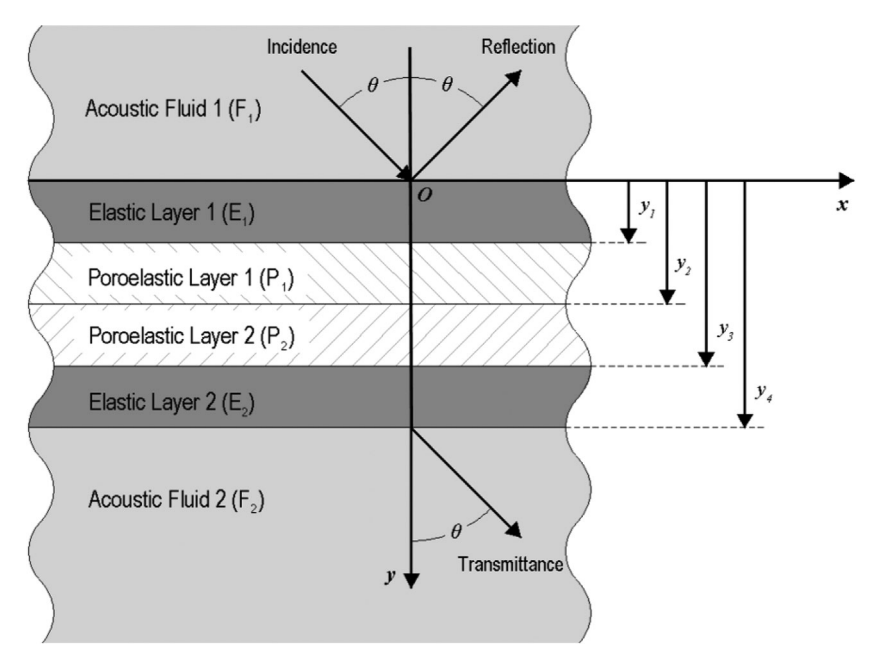


Figure 2. Schematic diagram for the laminated composite lay-up and sound transmission problem model.

www.aem-iournal.com

ADVANCED ENGINEERING MATERIALS

S- wavenumbers along the y-direction (i.e.,  $K_P^{(E)}$  and  $K_S^{(E)}$ )[23]:

$$u_{x}^{(E)} = ie^{-ik_{x}x} \left[ -k_{x} \left( C_{1}^{(E)} e^{iK_{p}^{(E)}\gamma} + C_{2}^{(E)} e^{-iK_{p}^{(E)}\gamma} \right) + K_{S}^{(E)} \left( C_{3}^{(E)} e^{iK_{S}^{(E)}\gamma} - C_{4}^{(E)} e^{-iK_{S}^{(E)}\gamma} \right) \right]$$
(5)

$$u_{\gamma}^{(E)} = i e^{-ik_{x}x} \left[ K_{p}^{(E)} \left( C_{1}^{(E)} e^{-iK_{p}^{(E)}y} + C_{2}^{(E)} e^{-iK_{p}^{(E)}y} \right) + K_{x} \left( C_{3}^{(E)} e^{iK_{S}^{(E)}y} - C_{4}^{(E)} e^{-iK_{S}^{(E)}y} \right) \right],$$

$$(6)$$

and

$$\begin{split} \sigma_{\gamma\gamma}^{(E)} &= -\mathrm{e}^{-\mathrm{i}k_{x}x} \Big[ 2\mu^{(E)}k_{x}K_{S}^{(E)} \Big( C_{3}^{(E)}\mathrm{e}^{\mathrm{i}K_{S}^{(E)}y} - C_{4}^{(E)}\mathrm{e}^{-\mathrm{i}K_{S}^{(E)}y} \Big) \\ &+ \Big( \lambda^{(E)}k_{x}^{2} + \Big( \lambda^{(E)} + 2\mu^{(E)} \Big) \Big( K_{P}^{(E)} \Big)^{2} \Big) \\ &\quad \cdot \Big( C_{1}^{(E)}\mathrm{e}^{\mathrm{i}K_{p}^{(E)}y} + C_{2}^{(E)}\mathrm{e}^{-\mathrm{i}K_{p}^{(E)}y} \Big) \Big], \end{split} \tag{7}$$

$$\begin{split} \sigma_{xy}^{(E)} &= \mu^{(E)} \mathrm{e}^{-\mathrm{i} k_x x} \bigg[ \bigg( (k_x)^2 - \bigg( K_p^{(E)} \bigg)^2 \bigg) \\ & \bigg( C_3^{(E)} \mathrm{e}^{\mathrm{i} K_S^{(E)} \gamma} + C_4^{(E)} \mathrm{e}^{-\mathrm{i} K_S^{(E)} \gamma} \bigg) \\ & - 2 k_x K_p^{(E)} \bigg( C_1^{(E)} \mathrm{e}^{\mathrm{i} K_p^{(E)} \gamma} - C_2^{(E)} \mathrm{e}^{-\mathrm{i} K_p^{(E)} \gamma} \bigg) \bigg], \end{split} \tag{8}$$

in which  $\lambda^{(E)}$  and  $\mu^{(E)}$  are the Lamé constant and shear modulus of the elastic medium, respectively,  $K_P^{(E)} = \sqrt{\left(\omega/c_P^{(E)}\right) - k_x^2}$ ,  $K_S^{(E)} = \sqrt{\left(\omega/c_S^{(E)}\right) - k_x^2}$ ,  $c_P^{(E)} = \sqrt{\lambda^{(E)} + 2\mu^{(E)}/\rho^{(E)}}$ , and  $c_S^{(E)} = \sqrt{\lambda^{(E)} + 2\mu^{(E)}/\rho^{(E)}}$ ,

 $\sqrt{\mu^{(E)}/\rho^{(E)}}$  are the wavenumbers and velocities of primary and secondary waves, respectively,  $\rho^{(E)}$  is the elastic solid material density and  $C_1^{(E)}$  to  $C_4^{(E)}$  are the elastic unknown coefficients. For the top elastic layer, the superscript (E) will be changed to (E<sub>1</sub>) and for the bottom one to (E<sub>2</sub>).

#### 3.3. Linear Poroelastic Medium

Elastic wave propagations in porous media are here analyzed using Biot's theory of dynamic poroelasticity. <sup>[24–26]</sup> According to this theory, the porous material is considered as a macroscopically homogeneous and isotropic two-phase solid/fluid material. The dilatational wave propagation in the solid phase can be expressed by a fourth order wave equation in terms of solid volumetric strain (i.e.,  $e^{(P)}$ ) as <sup>[27,28]</sup>:

$$\nabla^4 e^{(P)} + A_1^{(P)} \nabla^2 e^{(P)} + A_2^{(P)} e^{(P)} = 0, \tag{9}$$

where

$$A_{1}^{(P)} = \omega^{2} \Big( \rho_{11}^{*(P)} R^{(P)} - 2 \rho_{12}^{*(P)} Q^{(P)} + \rho_{22}^{*(P)} P^{(P)} \Big) / \Big( P^{(P)} R^{(P)} - (Q^{(P)})^{2} \Big), \tag{9a}$$

$$A_{2}^{(P)} = \omega^{4} \bigg( \rho_{11}^{*(P)} \rho_{22}^{\;*(P)} - \Big( \rho_{12}^{*(P)} \Big)^{2} \bigg) / \Big( P^{(P)} R^{(P)} - (Q^{(P)})^{2} \Big), \quad (9b)$$

$$P^{(P)} = A^{(P)} + 2N^{(P)}, (9c)$$

$$\rho_{11}^{*(P)} = \rho_1^{(P)} + \rho_a^{(P)} + b^{(P)}/i\omega, \tag{9d}$$

$$\rho_{12}^{*(P)} = -\rho_a^{(P)} - b^{(P)}/i\omega, \tag{9e}$$

$$\rho_{22}^{*(P)} = \rho_{2}^{(P)} + \rho_{a}^{(P)} + b^{(P)}/i\omega, \tag{9f}$$

in which  $A^{(P)}$  and  $N^{(P)}$  are the bulk in-vacuo Lamé constant and the shear modulus of the solid phase, respectively,  $Q^{(P)} = \left(1-h^{(P)}\right)E_2^{(P)}$ , is the coupling between fluid and solid phases,  $h^{(P)}$  is the material porosity, and  $E_2^{(P)}$  is the bulk modulus of elasticity for the fluid in the pores.  $R^{(P)}$ , here is assumed to be  $h^{(P)}$   $E_2^{(P)}$  and  $h^{(P)}$  is a viscous coupling factor related to the macroscopic flow resistivity of the porous material,  $\rho_1^{(P)}$  and  $\rho_2^{(P)} = h^{(P)}$   $\rho_0^{(P)}$  are the bulk densities of the solid and fluid phases, respectively, and  $\rho_a^{(P)} = \rho_2^{(P)} \left[ \left( \varepsilon' \right)^{(P)} - 1 \right]$  is the inertial coupling parameter between the fluid and solid phases. For cylindrical pores, the coefficient  $h^{(P)}$  can be expressed as  $h^{(P)'}$ 

$$\mathrm{i}\omega\epsilon^{(P)'} \rho_2^{(P)} \left(\frac{\rho_c^{*(P)}}{\rho_0^{(P)}} - 1\right)$$
 in which  ${\rho_c}^{*(P)}$  can be defined as<sup>[28]</sup>:

$$\rho_c^{*(P)} = \rho_0^{(P)} \left[ 1 - \frac{2J_1(\lambda_c^{(P)}\sqrt{-i})}{\lambda_c^{(P)}\sqrt{-iJ_0}(\lambda_c^{(P)}\sqrt{-i})} \right]^{-1}.$$
 (10)

where  $\left(\lambda_{\rm c}^{({\rm P})}\right)^2 = \frac{8\omega\rho_0^{({\rm P})}(\varepsilon')^{({\rm P})}}{h^{({\rm P})}\sigma^{({\rm P})}}, \ J_0 \ {\rm and} \ J_1 \ {\rm are} \ {\rm the} \ {\rm first} \ {\rm kind} \ {\rm Bessel}$  functions of zero and first orders, respectively. Also  $(\varepsilon')^{({\rm P})}$  is the geometrical structure factor and  $\sigma^{({\rm P})}$  is the steady state macroscopic flow resistivity of the porous material.

Two plane harmonic solutions for the Equation (9) can be obtained associated with the wavenumbers given by  $\left(k_{1,2}^{(P)}\right)^2 = \left(A_1^{(P)} \pm \sqrt{\left(A_1^{(P)}\right)^2 - 4A_2^{(P)}}\right)/2$ . The rotational wave

in the solid phase can be also expressed by another wave equation in terms of solid rotational strain (i.e.,  $\omega^{(P)}$ ) as [27,28]:

$$\nabla^2 \boldsymbol{\omega}^{(P)} + \left(k_t^{(P)}\right)^2 \boldsymbol{\omega}^{(P)} = 0, \tag{11}$$

where the wavenumber  $\left(k_t^{(P)}\right)^2 = \left(\omega^2/N^{(P)}\right)/\left(\rho_{11}^{*(P)}-\left(\rho_{12}^{*(P)}\right)^2/\rho_{22}^{*(P)}\right)$ . In Biot's theory, the volumetric and rotational strains in the fluid phase of the porous medium are determined in terms of the volumetric and rotational strains in the solid phase and, therefore, by solving wave equations, Equations 9 and 11, the strain fields in the fluid and solid phases both can be obtained (for more details, check [^{27,28}]). Consequently, by having the strain fields, the plane strain displacements for the solid (i.e.,  $u_x^{(P)}$  and  $u_y^{(P)}$ ) and fluid (i.e.,  $U_x^{(P)}$  and  $U_y^{(P)}$ ) phases can be obtained as follows  $[^{28,29}]$ :

www.aem-iournal.com

$$\begin{split} u_{\gamma}^{(P)} &= \mathrm{i} \mathrm{e}^{-\mathrm{i} k_{x} x} \Bigg[ \frac{k_{1\gamma}^{(P)}}{(k_{1}^{(P)})^{2}} C_{1}^{(P)} \mathrm{e}^{-\mathrm{i} k_{1\gamma}^{(P)} \gamma} - \frac{k_{1\gamma}^{(P)}}{(k_{1}^{(P)})^{2}} C_{2}^{(P)} \mathrm{e}^{\mathrm{i} k_{1\gamma}^{(P)} \gamma} \\ &+ \frac{k_{2\gamma}^{(P)}}{(k_{2}^{(P)})^{2}} C_{3}^{(P)} \mathrm{e}^{-\mathrm{i} k_{2\gamma}^{(P)} \gamma} - \frac{k_{2\gamma}^{(P)}}{(k_{2}^{(P)})^{2}} C_{4}^{(P)} \mathrm{e}^{\mathrm{i} k_{2\gamma}^{(P)} \gamma} \Bigg] \\ &+ \mathrm{i} \frac{k_{x}}{\left(k_{t}^{(P)}\right)^{2}} \mathrm{e}^{-\mathrm{i} k_{x} x} \bigg( C_{5}^{(P)} \mathrm{e}^{-\mathrm{i} k_{\eta}^{(P)} \gamma} + C_{6}^{(P)} e^{\mathrm{i} k_{\eta}^{(P)} \gamma} \bigg), \end{split} \tag{12-2}$$

$$\begin{split} U_{x}^{(P)} &= \mathrm{i} k_{x} \mathrm{e}^{-\mathrm{i} k_{x} x} \left[ \frac{b_{1}^{(P)} C_{1}^{(P)}}{\left(k_{1}^{(P)}\right)^{2}} \mathrm{e}^{-\mathrm{i} k_{1y}^{(P)} \gamma} + \frac{b_{1}^{(P)} C_{2}^{(P)}}{\left(k_{1}^{(P)}\right)^{2}} \mathrm{e}^{\mathrm{i} k_{1y}^{(P)} \gamma} + \frac{b_{2}^{(P)} C_{3}^{(P)}}{\left(k_{2}^{(P)}\right)^{2}} \mathrm{e}^{-\mathrm{i} k_{2y}^{(P)} \gamma} \right] \\ &+ \frac{b_{2}^{(P)} C_{4}^{(P)}}{\left(k_{2}^{(P)}\right)^{2}} \mathrm{e}^{\mathrm{i} k_{2y}^{(P)} \gamma} \right] - \mathrm{i} \mathrm{g}^{(P)} \frac{k_{ty}^{(P)}}{\left(k_{t}^{(P)}\right)^{2}} \mathrm{e}^{-\mathrm{i} k_{x} x} \\ &\left(C_{5}^{(P)} \mathrm{e}^{-\mathrm{i} k_{ty}^{(P)} \gamma} - C_{6}^{(P)} \mathrm{e}^{\mathrm{i} k_{ty}^{(P)} \gamma}\right), \end{split} \tag{12-3}$$

$$\begin{split} U_{\gamma}^{(P)} &= \mathrm{i}\mathrm{e}^{-\mathrm{i}k_{x}x} \Bigg[ \frac{b_{1}^{(P)}k_{1\gamma}^{(P)}C_{1}^{(P)}}{\left(k_{1}^{(P)}\right)^{2}} \mathrm{e}^{-\mathrm{i}k_{1\gamma}^{(P)}\gamma} - \frac{b_{1}^{(P)}k_{1\gamma}^{(P)}C_{2}^{(P)}}{\left(k_{1}^{(P)}\right)^{2}} \mathrm{e}^{\mathrm{i}k_{1\gamma}^{(P)}\gamma} \\ &+ \frac{b_{2}^{(P)}k_{2\gamma}^{(P)}C_{3}^{(P)}}{\left(k_{2}^{(P)}\right)^{2}} \mathrm{e}^{-\mathrm{i}k_{2\gamma}^{(P)}\gamma} - \frac{b_{2}^{(P)}k_{2\gamma}^{(P)}C_{4}^{(P)}}{\left(k_{2}^{(P)}\right)^{2}} \mathrm{e}^{\mathrm{i}k_{2\gamma}^{(P)}\gamma} \Bigg] \\ &+ \mathrm{i}\mathrm{g}^{(P)} \frac{k_{x}}{\left(k_{t}^{(P)}\right)^{2}} \mathrm{e}^{-\mathrm{i}k_{x}x} \Big( C_{5}^{(P)}\mathrm{e}^{-\mathrm{i}k_{t\gamma}^{(P)}\gamma} + C_{6}^{(P)}\mathrm{e}^{\mathrm{i}k_{t\gamma}^{(P)}\gamma} \Big), \quad (12\text{-}4) \end{split}$$

where

$$\left(k_{1,2y}^{(P)}\right)^2 = \left(k_{1,2}^{(P)}\right)^2 - k_{x}^2,$$
 (12a)

$$\left(k_{ty}^{(P)}\right)^2 = \left(k_t^{(P)}\right)^2 - k_x^2,$$
 (12b)

$$b_{1,2}^{(P)} = a_1^{(P)} - a_2^{(P)} \left(k_{1,2}^{(P)}\right)^2,$$
 (12c)

$$a_1^{(P)} = \left(\rho_{11}^{*(P)} R^{(P)} - \rho_{12}^{*(P)} Q^{(P)}\right) / \left(\rho_{22}^{*(P)} Q^{(P)} - \rho_{12}^{*(P)} R^{(P)}\right), \tag{12d}$$

$$a_{2}^{(P)} = \left(P^{(P)}R^{(P)} - \left(Q^{(P)}\right)^{2}\right) / \left(\omega^{2} \left[\rho_{22}^{*(P)}Q^{(P)} - \rho_{12}^{*(P)}R^{(P)}\right]\right), \tag{12e}$$

$$g^{(P)} = -\rho_{12}^{*(P)}/\rho_{22}^{*(P)}, \tag{12f}$$

and  $C_1^{(P)}$  to  $C_6^{(P)}$  are the unknown coefficients. The plain-strain stress components in the solid phase (i.e.,  $\sigma_{\gamma\gamma}^{(P)}$ ) and  $\sigma_{x\gamma}^{(P)}$ ) and the fluid pressure (i.e.,  $s^{(P)}$ ) in the fluid phase of the porous medium can be obtained from the Biot's stress-strain relationships as<sup>[28,29]</sup>:

$$\begin{split} \sigma_{\gamma\gamma}^{(P)} &= \mathrm{e}^{-\mathrm{i}k_{x}x} \left[ \left( 2N^{(P)} \frac{\left(k_{1\gamma}^{(P)}\right)^{2}}{\left(k_{1}^{(P)}\right)^{2}} + A^{(P)} + b_{1}^{(P)} Q^{(P)} \right) \\ & \left( C_{1}^{(P)} \mathrm{e}^{-\mathrm{i}k_{1\gamma}^{(P)}y} + C_{2}^{(P)} \mathrm{e}^{\mathrm{i}k_{1\gamma}^{(P)}y} \right) \\ & + \left( 2N^{(P)} \frac{\left(k_{2\gamma}^{(P)}\right)^{2}}{\left(k_{2}^{(P)}\right)^{2}} + A^{(P)} + b_{2}^{(P)} Q^{(P)} \right) \\ & \left( C_{3}^{(P)} \mathrm{e}^{-\mathrm{i}k_{2\gamma}^{(P)}y} + C_{4}^{(P)} \mathrm{e}^{\mathrm{i}k_{2\gamma}^{(P)}y} \right) \right] \\ & + 2N^{(P)} \frac{\left(k_{x}k_{t\gamma}^{(P)}\right)^{2}}{\left(k_{1}^{(P)}\right)^{2}} \left( C_{5}^{(P)} \mathrm{e}^{-\mathrm{i}k_{1\gamma}^{(P)}y} + C_{6}^{(P)} \mathrm{e}^{\mathrm{i}k_{1\gamma}^{(P)}y} \right), \end{split}$$

$$(13-1)$$

$$\begin{split} \sigma_{x\gamma}^{(P)} &= \mathrm{e}^{-\mathrm{i}k_{x}x} N^{(P)} \left[ \frac{2k_{x}k_{1\gamma}^{(P)}}{\left(k_{1}^{(P)}\right)^{2}} \left( C_{1}^{(P)} \mathrm{e}^{-\mathrm{i}k_{1\gamma}^{(P)}\gamma} - C_{2}^{(P)} \mathrm{e}^{\mathrm{i}k_{1\gamma}^{(P)}\gamma} \right) + \frac{2k_{x}k_{2\gamma}^{(P)}}{\left(k_{2}^{(P)}\right)^{2}} \\ & \left( C_{3}^{(P)} \mathrm{e}^{-\mathrm{i}k_{2\gamma}^{(P)}\gamma} - C_{4}^{(P)} \mathrm{e}^{\mathrm{i}k_{2\gamma}^{(P)}\gamma} \right) \right] + \frac{\left(k_{x}^{2} - \left(k_{t\gamma}^{(P)}\right)^{2}\right)}{\left(k_{t}^{(P)}\right)^{2}} \\ & \left( C_{5}^{(P)} \mathrm{e}^{-\mathrm{i}k_{t\gamma}^{(P)}\gamma} + C_{6}^{(P)} \mathrm{e}^{\mathrm{i}k_{t\gamma}^{(P)}\gamma} \right), \end{split} \tag{13-2}$$

$$\begin{split} s^{(P)} &= \mathrm{e}^{-\mathrm{i}k_{\mathrm{x}}x} \Big[ \Big( Q^{(P)} + b_{1}^{(P)} R^{(P)} \Big) \Big( C_{1}^{(P)} \mathrm{e}^{-\mathrm{i}k_{1y}^{(P)}y} + C_{2}^{(P)} \mathrm{e}^{\mathrm{i}k_{1y}^{(P)}y} \Big) \\ &+ \Big( Q^{(P)} + b_{2}^{(P)} R^{(P)} \Big) \Big( C_{3}^{(P)} \mathrm{e}^{-\mathrm{i}k_{2y}^{(P)}y} + C_{4}^{(P)} \mathrm{e}^{\mathrm{i}k_{2y}^{(P)}y} \Big) \Big]. \end{split} \tag{13-3}$$

Similar to the elastic layers, the superscript (P) will be changed to  $(P_1)$  for the top porous layer, and to  $(P_2)$  for the bottom one.

#### 3.4. Boundary Conditions

The unknown coefficients can be determined from appropriate boundary conditions imposed at the interfaces of each layer. These conditions are stated below<sup>[28]</sup>:

1) Fluid-Solid interfacial interactions at y = 0 and  $y = y_4$ :

$$i\omega u_{\nu}^{(E_{1,2})} = \nu_{\nu}^{(F_{1,2})}, \tag{14-1} \label{eq:14-1}$$

$$\sigma_{yy}^{(E_{1,2})} = -p^{(F_{1,2})}, \tag{14-2}$$

$$\sigma_{xy}^{(E_{1,2})} = 0, \tag{14-3}$$

www.advancedsciencenews.com www.aem-iournal.com

2) Solid-Porous interfacial interactions at  $y = y_1$  and  $y_3$ :

$$u_{\mathbf{x}}^{(\mathbf{E}_{1,2})} = u_{\mathbf{x}}^{(\mathbf{P}_{1,2})},$$
 (15 – 1)

$$u_{\gamma}^{(E_{1,2})} = u_{\gamma}^{(P_{1,2})}, \tag{15-2} \label{eq:15-2}$$

$$u_{\gamma}^{(E_{1,2})} = U_{\gamma}^{(P_{1,2})},$$
 (15 – 3)

$$\sigma_{\gamma\gamma}^{(E_{1,2})} = \left(1 - h^{(P_{1,2})}\right) \sigma_{\gamma\gamma}^{(P_{1,2})} - h^{(P_{1,2})} s^{(P_{1,2})}, \tag{15-4} \label{eq:15-4}$$

$$\sigma_{xy}^{(E_{1,2})} = \left(1 - h^{(P_{1,2})}\right) \sigma_{xy}^{(P_{1,2})}, \tag{15-5}$$

3) Porous-Porous interfacial interaction at  $y = y_2$ :

$$u_x^{(P_1)} = u_x^{(P_2)}, (16-1)$$

$$u_{\gamma}^{(P_1)} = u_{\gamma}^{(P_2)}, \tag{16-2}$$

$$h^{(P_1)}\Big(u_{\gamma}^{(P_1)}-U_{\gamma}^{(P_1)}\Big)=h^{(P_2)}\Big(u_{\gamma}^{(P_2)}-U_{\gamma}^{(P_2)}\Big), \tag{16-3}$$

$$\sigma_{\gamma\gamma}^{(P_1)} - s^{(P_1)} = \sigma_{\gamma\gamma}^{(P_2)} - s^{(P_2)}, \tag{16-4} \label{eq:16-4}$$

$$\sigma_{xy}^{(P_1)} = \sigma_{xy}^{(P_2)}, \tag{16-5}$$

$$h^{(P_1)}s^{(P_1)} = h^{(P_2)}s^{(P_2)}. (16-6)$$

Equations 14 to 16 can be readily written in a matrix form as:

$$[\mathbf{M}]_{22\times22}[\mathbf{X}]_{22\times1} = [\mathbf{B}]_{22\times1},\tag{17}$$

in which

$$[X]^{T} = [C_{1}^{(E_{1})}...C_{4}^{(E_{1})}C_{1}^{(E_{2})}...C_{4}^{(E_{2})}C_{1}^{(P_{1})}...C_{6}^{(P_{1})}C_{1}^{(P_{1})}...C_{6}^{(P_{2})}I_{R}I_{T}],$$
(17a)

where  $[X]^T$  is the transpose of X. Therefore, the reflected  $(I_R)$  and transmitted  $(I_T)$  sound intensities as a function of incident angle and frequency can be obtained by solving Equation 17.

#### 3.5. Diffuse Sound Transmission Loss

Sound transmission loss is defined as<sup>[22]</sup>:

$$STL(dB) = 10log_{10}(1/\tau), \tag{18}$$

where the sound transmission coefficient,  $\tau(\omega, \theta) = |I_T|^2/|I_I|^2$ , is the ratio of the transmitted intensity to the incident intensity. Here the incident sound wave is considered to have a unit amplitude. In a diffuse field, it is required to consider an angle-averaged diffuse-field transmission coefficient (i.e.,  $\tau_d$ ), which

the angular characteristics of the incident wave energy are taken into account, defined as<sup>[30]</sup>:

$$\tau_{d} = \frac{\int_{0}^{\pi/2} G(\theta)\tau(\omega,\theta)\cos\theta\sin\theta d\theta}{\int_{0}^{\pi/2} G(\theta)\cos\theta\sin\theta d\theta},$$
(19)

where  $G(\theta) = \mathrm{e}^{-\beta\theta^2}$  is the normalized Gaussian weighing function. For a perfect diffuse field,  $\beta = 2.^{[31]}$  The integral equation in Equation 19 can be numerically evaluated. Here, it should be noted that the transmission loss cannot be determined exactly at  $\theta = \pi/2$  due to a singularity in the theory of elasticity. [32]

#### 3.6. Materials Parameterization

A systematic approach for the aerogel material parameterization has been previously proposed and validated by the authors.  $^{[18]}$  In this approach, all required material parameters for this class of PUA aerogels are estimated mainly based on the aerogel bulk density. Some physical characteristics such as skeletal density, average pore size diameter ( $\Gamma$ ) and Poisson's ratio ( $\nu$ ) of the aerogels are considered to remain unchanged with the variation of the aerogel bulk density. This assumption is mainly the outcome of the previous co-author's investigations on the physical behavior of the PUA aerogels at different bulk densities.  $^{[12]}$  Table 1 lists the aerogel physical parameters that were used in this study.

The remaining material parameters are related to the gypsum and air. The gypsum material parameters and air properties are listed in Table 2.

#### 4. Results and Discussion

The morphology and the size distribution of the PUA aerogels are shown in Figure 3. The SEM images reveal a nano-fibrous

**Table 1.** The PUA aerogel material parameters used in the present calculations.

Bulk density ( $\rho_b$ , g cm <sup>-3</sup> )	0.15	0.25		
Skeletal density ( $\rho_{\rm s}$ , g cm $^{-3}$ )	1.24	1.24		
Porosity ( $h = (\rho_s - \rho_b)/\rho_s$ )	0.88	0.80		
Average pore size diameter (Γ, nm)	40.33	40.33		
Static Young's modulus $(E_1 = 967.94 \rho_b^{2.004}, MPa)^a)$	22.20	61.78		
Average Poisson's ratio (ν)	0.22	0.22		
Young's modulus loss factor $(\eta)^{b}$ i.e., $E_1(1+i\eta)$	0.125	0.125		
Geometrical structure factor (ε') b)	netrical structure factor (ɛ') <sup>b)</sup>			
Air flow resistivity ( $\sigma = 8\mu/\Gamma^2 h$ , Ns m $^{-4}$ ) $^{c)}$	$1.03\times10^{11}$	$1.13\times10^{11}$		

a) Refs.[18,33]

b) Ref.[34]

c) Ref.[28]

www.aem-iournal.com

MATERIALS

**Table 2.** The gypsum and air material parameters used in the present calculations.

Gypsum bulk density (g cm <sup>-3</sup> )	1
Gypsum Young's modulus (GPa)	2
Gypsum Poisson's ratio	0.33
Air density ( $\rho_0$ , kg m <sup>-3</sup> )	0.909
Speed of sound in air $(m s^{-1})$	328.6
Shear viscosity ( $\mu$ , Ns m $^{-2}$ )	$1.84\times10^{-5}$
Prandtl number of air (Pr)	0.715
Ratio of air specific heats (γ)	1.2

structure for both 0.15 g cm<sup>-3</sup> (Figure 3a) and 0.25 g cm<sup>-3</sup> (Figure 3c) densities. The pore structures are highly random in both samples. However, the structure for higher bulk density aerogel is relatively more packed in comparison with the lower density sample. This leads to a lower porosity for higher bulk density sample in agreement with our previous porosity estimations using skeletal and bulk densities. Higher resolution images are also provided as onsets of the SEM images. The fiber diameter distributions are also obtained for both samples as shown in Figure 3b and d. The average diameter for the higher bulk density sample is lower and more uniformly distributed over the sample which indicates the consistency of the synthesis protocol.

The airborne STL values for the two sets of samples at frequency range of 100–5000 Hz are obtained within an ASTM E90 test chamber. Results for the 1 m<sup>2</sup> sample set are shown in **Figure 4**. A significant increase can be seen over the entire frequency range, remarkably at 4 kHz with more than 15 dB, due to the aerogel constraint layers. The dip in the STL values of the gypsum-only panel at 4 kHz can be explained using thin plate

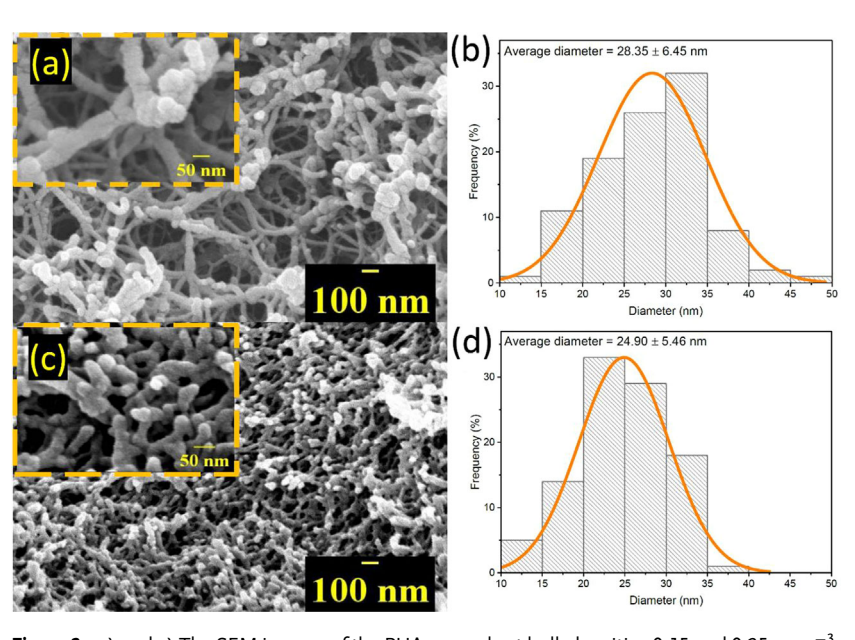


**Figure 3.** a) and c) The SEM images of the PUA aerogels at bulk densities 0.15 and 0.25 g cm $^{-3}$ , respectively; b) and d) The fiber diameter size distributions of the PUA aerogel networks at bulk densities 0.15 and 0.25 g cm $^{-3}$ , respectively.

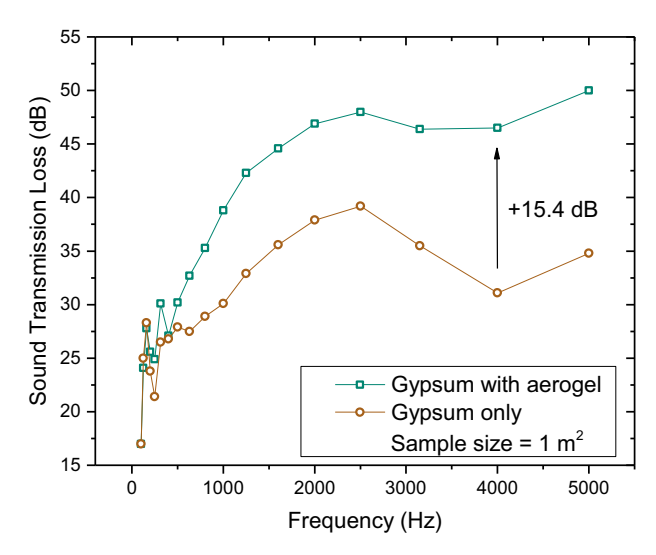


Figure 4. The effect of PUA aerogels on the airborne STL values of 1 m<sup>2</sup> samples as a function of frequency.

theory.<sup>[35]</sup> According to this theory, for an unbounded flexible partition, at a certain frequency, the incident wave is coincident with the bending wave in the partition. This coincidence frequency ( $f_c$ ) is approximated as<sup>[35]</sup>:

$$f_c = \frac{c_0^2}{2\pi \sin^2 \theta} \sqrt{\frac{\rho t_0}{D}},\tag{20}$$

where  $D = E_0 t_0^3 / 12 (1 - \nu_0^2)$ , is the partition's bending stiffness with  $E_0$ ,  $\nu_0$ , and  $t_0$  being the Young's modulus, the Poisson's ratio and the thickness of the partition, respectively. Using Equation 20, the estimated coincidence frequencies for an unbounded

gypsum panel at incident angles less than 90° are entirely above 2000 Hz. Consequently, the dip at 4 kHz in the experimental values of the STL can be correlated to the lowest coincidence frequency of the gypsum only partition. Therefore, one can say that the aerogel implementation not only caused the corresponding coincidence effect to be disappeared, but also increased the STL values from 30 to 45 dB at this frequency. It should be also emphasized that this unusual enhancement was obtained only with 20% increase in the overall mass of the test sample. According to the Mass Law, by 20% increase in the mass per unit area of a partition, we can only expect to improve the STL values by 1.5 dB while the aerogel utilization can increase the STL values by a factor of 10. It should be mentioned that the STL recovery at the coincidence frequency is due to the aerogel constraint damping effects. Such effects might be originated from the damping property of the aerogel's solid phase (loss factor of polyurea) and the viscous damping property between the fluid and solid phases (viscous coupling factor between air

www.aem-iournal.com

ADVANCED ENGINEERING MATERIALS

and polyurea). The STL enhancements at different frequencies as well as the sound transmission classes (STC)<sup>[36]</sup> are listed in **Table 3**. This finding opens a door to various applications where high STL is required.

In order to further validate and better capture the actual physical effects of the aerogels, the finite boundary effects including sample in-place mounting mechanisms and sample frame holder effects must be minimized. One way to accomplish this, is to provide a bigger test sample. Therefore, through a systematically consistent experiment with previous trials, another experiment was carried out to measure the airborne STL values of a 10 m<sup>2</sup> test sample. Since the incidence area of this set is 10 times bigger than the first set, we can expect that all boundary effects should be minimized and therefore we can capture the true core effects and obtain more realistic environmental test situation. The obtained STL results of the 10 m<sup>2</sup> gypsum-only and gypsum-aerogel composite samples are depicted in Figure 5. Interestingly, the results for both 1 and 10 m<sup>2</sup> test sets are containing very similar trends which proves the consistency and high reproducibility of the executed material preparation and acoustic test methods. The size insensitivity of the STL and/or STC enhancement due to the low-density aerogel layers confidently provides several potential advanced engineering applications for these hierarchical class of materials (check Table 3).

We have previously showed the feasibility of the Biot's dynamic poroelasticity on the modeling of the normal incidence STL of the single layer PUA aerogels at different bulk densities. [18] In order to recheck the applicability of the Biot's theory on the wave propagation problems including the aerogel materials, here the modeling methodology was extended to a multilayered composite material with the help of theory of elasticity and acoustics field theory. The two-dimensional plane strain analytical solution along with the experimental airborne STL values for both 1 and 10 m<sup>2</sup> layered composite samples are shown in Figure 6. The analytical results provide an excellent agreement with the experimental results over the entire frequency range, reassuring the feasibility of this technique to model the aerogel-based dynamic systems and structures. It is worth mentioning that the typical porous material parameterizations are rigorously experimentally involved in order to reach meaningful results in comparison with experiments, However,

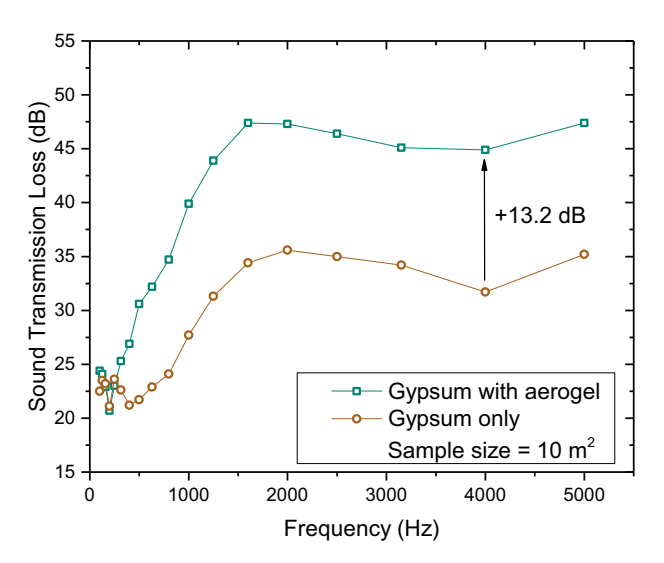


Figure 5. The effect of PUA aerogels on the airborne STL values of 10 m<sup>2</sup> samples as a function of frequency.

in this research, a relatively simple and straightforward material parameterization approach has been taken into account which was mainly limited to the bulk density and Young's modulus measurements. Therefore, the theory-experiment agreement in this work on the wave propagation properties of the layered composites can be considered as a parameter sensitivity analysis for other material parameterization techniques.

Relying on the predicted analytical results, the effects of average core bulk density on the insulation properties of the layered composites was investigated and results are shown in Figure 7. The bulk density ratio of the two aerogel layers was kept to 1.5 for all calculations and results are depicted as a function of frequency at different average aerogel bulk densities. Such calculation is necessary for the purpose of design and optimizations. At low frequency range (less than 1 kHz), the increase in the core density consistently enhances the STL. However, the coincidence frequency is shifting to the lower frequencies by increasing the core density. Therefore, the STL for the heavier panels in contrast with the lighter panels is starting to decrease at lower frequencies due to the coincidence

Table 3. The STL values and enhancements (STL-E) at different frequencies and the sound transmission classes (STC) of gypsum and gypsum-aerogel composite panels, all in dB, at different sizes.

Freq. (Hz)		STL	STL-E <sup>a)</sup>		STL	STL-E
1000	30.1	38.8	8.7	27.7	39.9	12.2
2000	37.9	46.9	9.0	35.6	47.3	11.7
3150	35.5	46.4	10.9	34.2	45.1	10.9
4000	31.1	46.5	15.4	31.7	44.9	13.2
5000	34.8	50	15.2	35.2	47.4	12.2
STC <sup>b)</sup>	31	36	-	28	34	-
Panel	Gypsum (1 m²)	Composite (1 m²)	-	Gypsum (10 m²)	Composite (10 m²)	-

<sup>&</sup>lt;sup>a)</sup> STL-E = STL (Composite) - STL (Gypsum)

b) In compliance with ASTM E413<sup>[36]</sup>



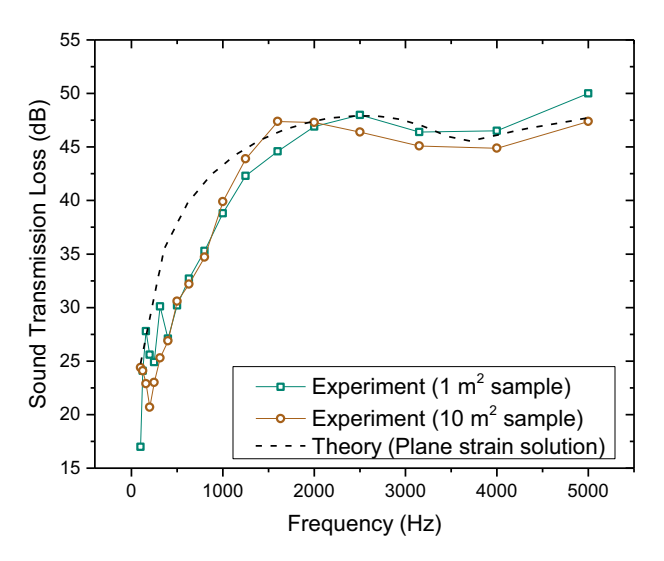


**Figure 6.** The comparison between the plane strain theoritical solution with experimental airborne STL values of gypsum-aerogel composite samples as a function of frequency at different sizes.

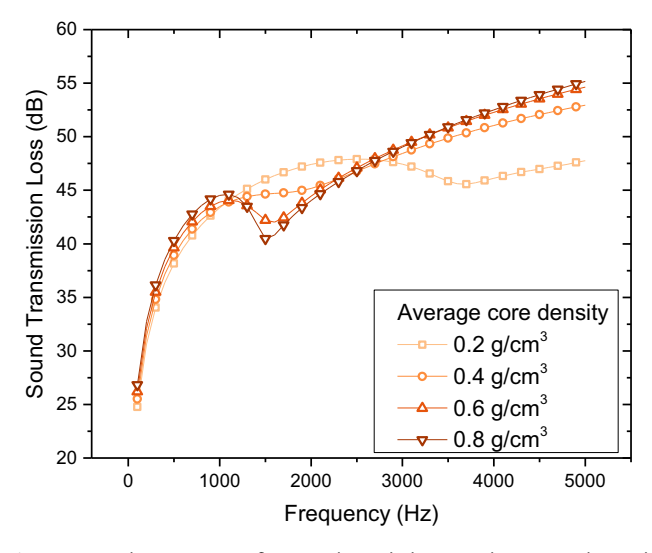


**Figure 7.** Airborne STL of an unbounded aerogel-gypsum layered composite as a function of frequency at different average core bulk densities (the ratio of the two aerogel bulk densities was kept to 1.5).

effect. This decrease in the frequency of the coincidence effect is associated to the increase in the overall bending stiffness of the composite with increasing the core bulk density, check Equation 20.

## 5. Conclusions

In this work, an inorganic-organic layered composite comprising low-density nanoporous PUA aerogels with gypsum material was considered. Within two independent sets of experiments, the chamber-based airborne STL of the composite samples were measured. The constraint effects of the aerogel layers were studied in both experiments and the results demonstrated

consistently a significant increase in the airborne STL of the layered composite structures. Due to the slight structural weight change by applying the low-density multifunctional PUA aerogels, this uncommon STL enhancement clearly breaks the empirical mass law in sound insulation behavior of conventional acoustics materials. Owing to their low thermal conductivity, low-cost and facile molding and machining of this type of organic aerogel materials, it is envisioned that they will become attractive at several advanced engineering scenes where extreme sound and/or heat insulations are required.[17,18] Finally, a 2D plane strain analytical solution was provided to model the wave propagations through the layered composite material. Excellent agreement with the experimental observations was obtained that shows the applicability of the proposed methodology for the aim of design and optimization of similar hierarchical and future low-density aerogel based dynamic applications and technologies.

## **Acknowledgements**

The support by AFOSR FA9550-14-1-0227, NSF CMMI-1636306, CMMI-1661246, and ECCS-1307997, and Nashi New Materials, Inc. China is acknowledged. N. L. and C. S.-L. thank the Army Research Office for financial support under Award Number W911NF-14-1-0369, and Covestro LLC (formerly Bayer Corporation U.S.A.) for the generous supply of Desmodur N3300A. H. L. also thanks the Luis A. Beecherl Jr. Chair for additional support. We also thank Mr. Zhicheng Liu and Mr. Qingrong Zhao for the preparation of the experimental setup.

#### **Conflict of Interest**

The authors declare no conflict of interest.

## **Keywords**

Biot's poroelasticity, composite structures, diffuse field sound transmission loss, nanoporous materials; polyurea aerogel

Received: October 24, 2017 Revised: January 22, 2018 Published online:

- [1] R. F. Gibson, Compos. Struct. 2010, 92, 12.
- [2] S. Gasser, Y. Brechet, F. Paun, Adv. Eng. Mater. 2004, 6, 12.
- [3] L. Tong, A. P. Mouritz, M. K. Bannister, 3D Fibre Reinforced Polymer Composites, Elsevier, Oxford 2002.
- [4] I. O. Golosnoy, J. C. Tan, T. W. Clyne, Adv. Eng. Mater. 2008, 10, 3.
- [5] A. C. Pierre, in Aerogels Handbook (Eds: M. A. Aegerter, N. Leventis, M. M. Koebel), Springer, New York 2011, Ch. 1.
- [6] A. C. Pierre, G. M. Pajonk, Chem. Rev. 2002, 102, 11.
- [7] F. Sabri, M. E. Sebelik, R. Meacham, J. D. Boughter, M. J. Challis, N. Leventis, PLoS ONE 2013, 8, 6.
- [8] N. Leventis, C. Sotiriou-Leventis, G. Zhang, A.-M. M. Rawashdeh, Nano Lett. 2002, 2, 9.
- [9] A. C. Pierre, A. Rigacci, in *Aerogels Handbook* (Eds: M. A. Aegerter, N. Leventis, M. M. Koebel), Springer, New York 2011, Ch. 2.
- [10] M. A. B. Meador, L. A. Capadona, L. McCorkle, D. S. Papadopoulos, N. Leventis, Chem. Mater. 2007, 19, 9.
- [11] X. Lu, M. C. Arduini-Schuster, J. Kuhn, O. Nilsson, J. Fricke, R. W. Pekala, *Science* 1992, 255, 5047.



www.aem-iournal.com



- [12] a) N. Leventis, C. Sotiriou-Leventis, N. Chandrasekaran, S. Mulik, Z. J. Larimore, H. Lu, G. Churu, J. T. Mang, Chem. Mater. 2010, 22, 24; b) A. S. Lee, Synthesis and Mechanical Characterization of Mesoporous Polyurea, The University of Texas at Dallas, ProQuest Dissertations Publishing, Ann Arbor 2014.
- [13] C. Chidambareswarapattar, P. M. McCarver, H. Luo, H. Lu, C. Sotiriou-Leventis, N. Leventis, Chem. Mater. 2013, 25, 15.
- [14] C. Chidambareswarapattar, L. Xu, C. Sotiriou-Leventis, N. Leventis, RSC Adv. 2013, 3, 48.
- [15] N. Leventis, C. Chidambareswarapattar, D. P. Mohite, Z. J. Larimore, H. Lu, C. Sotiriou-Leventis, J. Mater. Chem. 2011, 21, 11981.
- [16] H. Lu, H. Luo, N. Leventis, in Aerogels Handbook (Eds: M. A. Aegerter, N. Leventis, M. M. Koebel), Springer, New York 2011, Ch. 22.
- [17] H. Lu, N. Xiang, N. Leventis, C. Sotiriou-Leventis, US Patent 14059254, 2013.
- [18] S. Malakooti, H. G. Churu, A. Lee, T. Xu, H. Luo, N. Xiang, C. Sotiriou-Leventis, N. Leventis, H. Lu, J. Non Cryst. Solids 2017, 476, 36.
- [19] B. Hinze, J. Rösler, Adv. Eng. Mater. 2014, 16, 3.
- [20] Standard test method for laboratory measurement of airborne aound transmission loss of building partitions and elements, ASTM International, ASTM E90, 2016.
- [21] Acoustics: measurement of sound insulation in buildings and of building elements, International Organization for Standardization, ISO 140, 2004.

- [22] A. D. Pierce, Acoustics: An Introduction to Its Physical Principles and Applications, McGraw-Hill Book Co, New York 1981.
- [23] K. F. Graff, Wave Motion in Elastic Solids, Dover Publications, Oxford 1991.
- [24] M. A. Biot, J. Acoust. Soc. Am. 1956, 28, 2 (Part I).
- [25] M. A. Biot, J. Acoust. Soc. Am. 1956, 28, 2 (Part II).
- [26] M. A. Biot, J. Appl. Phys. 1962, 33, 4.
- [27] T. Bourbié, O. Coussy, B. Zinszner, Acoustics of Porous Media, Gulf Publishing Co., 1987.
- [28] J.-F. Allard, N. Atalla, Propagation of Sound in Porous Media: Modelling Sound Absorbing Materials, Wiley, Chichester 2009.
- [29] J. S. Bolton, N.-M. Shiau, Y. J. Kang, J. Sound Vib. 1996, 191, 3.
- [30] H.-J. Kang, J.-G. Ih, J.-S. Kim, H.-S. Kim, J. Acoust. Soc. Am. 2000, 107. 3.
- [31] A. Pellicier, N. Trompette, Appl. Acoust. 2007, 68, 10.
- [32] S. Chonan, Y. Kugo, J. Acoust. Soc. Am. 1991, 89, 2.
- [33] H. Fan, C. Hartshorn, T. Buchheit, D. Tallant, R. Assink, R. Simpson, D. J. Kissel, D. J. Lacks, S. Torquato, C. J. Brinker, *Nature Mater.* 2007, 6. 6.
- [34] J. Qiao, A. V. Amirkhizi, K. Schaaf, S. Nemat-Nasser, G. Wu, Mech. Mater. 2011, 43.
- [35] F. Fahy, P. Gardonio, Sound and structural vibration: radiation, transmission and response, Elsevier, 2007.
- [36] Classification for rating sound insulation, ASTM International, ASTM E413, 2016.